Microscopic liquid-gas interface effect on liquid wetting

Zhang, J.; Ding, W.; Wang, Z.; Wang, H.; Hampel, U.;

Perma-Link to Publication Repository of HZDR:

https://www.hzdr.de/publications/Publ-35321

Microscopic liquid-gas interface effect on liquid wetting

Jinming Zhang[a], Wei Ding[a,*], Zuankai Wang[c], Hao Wang[d], Uwe Hampel[a,b]

[a]Helmholtz-Zentrum Dresden-Rossendorf (HZDR), Institute of Fluid Dynamics, Dresden 01328, Germany

[b]Technische Universität Dresden, Institute of Power Engineering, Dresden 01062, Germany

[c]Department of Mechanical Engineering, City University of Hong Kong, Hong Kong SAR 999077, China

[d]The Laboratory of Heat and Mass Transport at Micro-Nano Scale, College of Engineering, Peking University, Beijing 100871, China

Jinming Zhang email address: j.zhang@hzdr.de

Wei Ding email address: w.ding@hzdr.de

Zuankai Wang email address: zuanwang@cityu.edu.hk

Hao Wang email address: hwang@coe.pku.edu.cn

Uwe Hampel email address: u.hampel@hzdr.de

Corresponding Author

Wei Ding - Helmholtz-Zentrum Dresden-Rossendorf (HZDR), Institute of Fluid Dynamics, Dresden 01328, Germany; Email: w.ding@hzdr.de

Phone: +49-351-260 2170

FAX: +49 351 260 2383

Abstract:

Hypothesis: Young contact angle is widely applied to evaluate liquid wetting phenomena on solid surfaces. For example, it gives a truncated-spherical shape prediction of a droplet profile through the Young-Laplace equation. However, recent measurements have shown deviations between microscopic droplet profiles and the spherical shape, indicating that the conventional Young contact angle is insufficient to describe microscopic wetting phenomena. In this work, we hypothesize that a liquid-gas interface nano-bending, which is caused by the nonlinear coupling between the effects of the microscopic interface geometry and solid-liquid interactions, is responsible for this deviation.

Simulation and theory: Using molecular dynamics simulations and mathematical modeling, we reveal the structure of the nano-bending and the mechanism of the nonlinear-coupled effect. We further apply our findings to illustrate a liquid microlayer with the saddle-shaped profile in nucleate boiling.

Findings: The nonlinear-coupled effect is responsible for the deviation of a nano-droplet profile and also the very thin microlayer captured by different experiments. The saddle-shaped interface significantly highlights the nonlinear-coupled effect. The interface nano-bending, rather than the Young contact angle, acts as the boundary condition and dictates the liquid wetting system, especially for the case with high interface curvature. These findings provide insight into recent nano-scale droplet- and bubble-related wetting phenomena.

KEYWORDS: liquid wetting, nano-bending, nonlinear-coupled effect, interface curvature, Young contact angle, nano-droplet, nano-bubble, microlayer, nucleate boiling

1. Introduction

Liquid wetting on surfaces is ubiquitous in nature and is of great scientific and technological interest [1–4]. Recent examples such as liquid directional steering [5], surface curvature-driven droplet motion [6], ultra-thin water film evaporation [7,8], and triboelectric nanogenerators [9,10] have illustrated the beauty of the wetting phenomena by tailoring the solid surface properties,

47 including curvature, roughness, and chemistry. Despite its seeming simplicity, understanding these

48 intriguing liquid-wetting behaviors requires probing the complex solid-liquid interaction that

49 manifests itself as the contact angle [11].

50 Conventionally, the Young contact angle is central to describing a wetting system since it

51 provides the critical boundary condition for the bulk liquid [12,13]. For example, the equilibrium

52 droplet profile on an ideal surface is dictated by the Young contact angle through the Young-

53 Laplace equation

54 $$P_g - P_l = P_c,$$ (1)

55 in which P_g and P_l are the pressure in the gas and liquid phase. P_c is the capillary pressure induced

56 by the interface curvature $P_c = \sigma K$. σ is the liquid-gas interface surface tension, and K is the

57 interface curvature. The prediction of Eq. 1 provides a truncated-spherical shape of the droplet

58 profile. On the contrary, experimentally observed nano-scale droplet profiles have always

59 exhibited a meniscus within 20 nm thickness from the contact line even on smooth and

60 homogeneous surfaces [14–16]. This deviates from the prediction based on the Young contact

61 angle. In a recent experimental measurement of the nano-droplet profile, Samoila *et al.* obtained

62 completely different contact angles of the nano-droplets with different volumes on the same

63 surface [17]. This indicates that the Young contact angle as the boundary condition is insufficient

64 to describe the nano-scale wetting phenomena. Therefore, an exact mechanism to explain the

65 deviation can be crucial to numerous nano-scale wetting-related phenomena, *e.g.,* interfacial mass

66 transport [18,19] and contact line dynamics [20,21].

67 To account for this deviation, the effect of the solid-liquid molecular interaction [17,19,22]

68 near the contact line has been investigated extensively. The solid-liquid interaction gives rise to

69 the scale-dependent surface molecular forces and distorts the gas-liquid interface. In addition, the

70 contact angle of a droplet below a critical size has been found dependent on the droplet size

71 [16,23,24], *i.e.,* the line tension effect. Although descriptions of both effects have been well

72 established in the past decades, there seems to exist an internal connection that is still confusing.

73 Indeed, surface molecular forces can strongly influence the interface curvature [25]. On the other

74 hand, the line tension, as a manifestation of surface molecular forces near the contact line, is

75 dependent on the curvature of the gas-liquid interface [26,27]. Interestingly, a recent molecular

3

76　dynamics (MD) simulation suggested that the effect of gas-liquid interface curvature and the effect

77　of surface molecular forces are entangled [28]. This is not surprising given that these two effects

78　have an identical origin, *i.e.,* molecular interactions [29]. However, the entanglement brings

79　difficulties in understanding how a nano-scale droplet profile deviates. An insight into the

80　entangled relationship between the effect of surface molecular forces and the effect of the gas-

81　liquid interface curvature is needed.

82　The interface curvature of a 3D axisymmetric droplet is characterized by two principal

83　curvatures κ_1, κ_2 as $K = \kappa_1 + \kappa_2 = \dfrac{\delta''}{(1+\delta'^2)^{\frac{3}{2}}} + \dfrac{\delta'}{r(1+\delta'^2)^{\frac{1}{2}}}$ (**Fig. 1a**). δ represents the height of the

84　droplet profile, and r is the radius. However, the principal curvatures of a droplet have the same

85　signs: $\kappa_1\kappa_2 > 0$, that is, the capillary pressure caused by both principal curvatures increases the

86　liquid pressure and promotes the formation of a spherical droplet. In this case, the deviation of an

87　actual droplet profile only occurs at the microscopic scale, thus veiling the physics of the entangled

88　effect.

89　An interesting case of a surface wetting configuration with principal curvatures of different

90　signs is the microlayer in the inertia-controlled bubble growth stage in nucleate boiling, which is

91　a μ-meter thin liquid film trapped underneath a rapidly growing bubble. Besides being of practical

92　importance for heat transfer applications [30–32], the microlayer is a good example to illustrate

93　the entangled effect of the contact line geometry and surface molecular forces. Unlike the spherical

94　droplet (**Fig. 1a**), the 3D profile of the microlayer is saddle-shaped (**Fig. 1b**) and $\kappa_1\kappa_2 < 0$. In this

95　case, the capillary pressure induced by interface curvatures can be understood to both increase and

96　decrease the liquid pressure, depending on the direction of the principal curvature.

97　The accurate description of the microlayer has been a challenge for decades. Previous works

98　mainly resort to DNS simulations and mechanistic models to tackle the hydrodynamic part of this

99　problem [31,33–35], which failed to explain the very thin microlayer obtained in recent

100　experiments [36–38]. It is also worthy mentioning that some recent microlayer simulations have

101　achieved comparable thickness with the experiment results by considering the effects of

102　microlayer evaporation [39–41] and contact line dewetting [42,43]. Nevertheless, the obvious

103　microlayer evaporation and the contact line dewetting were observed only after the early stage

104　[36,44,45], referred to as the diffusion-controlled bubble growth stage [46].

105   This work aims to reveal how the effect of surface molecular forces and the effect of the gas-
106   liquid interface curvature are entangled. We first studied the entangled effects on the deviation of
107   a 3D nano-droplet profile by using MD simulations. Then we developed a three-region description
108   of the microlayer (**Fig. 1b**) that considers the entangled effects of surface molecular forces and
109   gas-liquid interface curvature. We elucidated the relationship between the effect of surface
110   molecular forces and the effect of the gas-liquid interface curvature. We found that the mechanism
111   responsible for the deviation of a nano-droplet profile can explain the very thin microlayer, though
112   the detailed manifestations of the entanglement are different in the context of the nano-droplet and
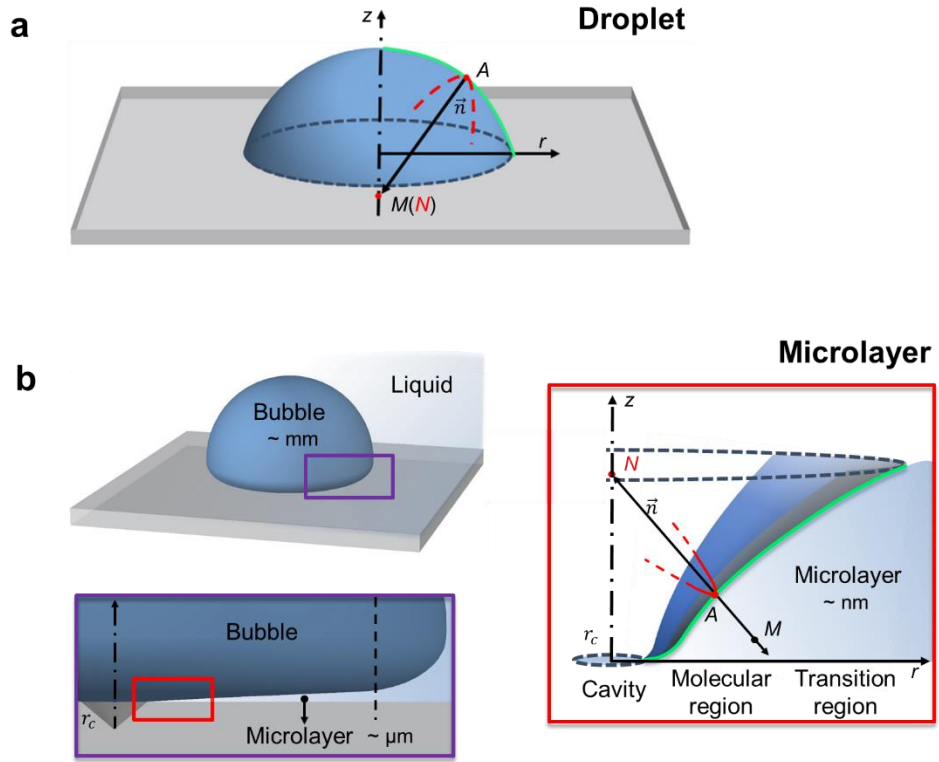113   microlayer.

114

115   **Fig. 1. Geometry configurations of surface wetting examples.** (**a**) Schematic of a 3D droplet
116   on a solid surface. $\overrightarrow{AM}$ and $\overrightarrow{AN}$ are the radii of the principal curvatures κ_1 and κ_2 of the gas-liquid
117   interface (Green line). (**b**) Schematic of a 3D multiscale microlayer underneath a growing bubble
118   in the inertia-controlled bubble growth stage in nucleate boiling. The microlayer consists of a
119   molecular region, a transition region, and a hydrodynamic region. The molecular region starts from
120   the edge of a cavity, followed by the transition region and the hydrodynamic region of the

121 microlayer. r_c is the radius of the cavity. $\overrightarrow{AM}$ and $\overrightarrow{AN}$ are the radii of the principal curvatures κ_1

122 and κ_2 of the microlayer vapor-liquid interface (Green line).

2. Methods

2.1 Molecular dynamics simulation

125 The equilibrium 3D nano-droplets on silicon (1 0 0) substrate are simulated to investigate the

126 entangled effect of surface molecular forces and the interface curvature by using MD simulations

127 via the LAMMPS software package [47]. Specifically, we vary the footprint radii of the droplet (5

128 nm, 7.5 nm, and 10 nm) to account for the effect of the interface curvature. The surface molecular

129 forces between water molecules and silicon atoms are modeled by the 12-6 L-J potential via silicon

130 and oxygen atoms with the parameters $\sigma_{Si-O} = 3.41$ Å and $\varepsilon_{Si-O} = 1.457$ KJ/mol [48]. The water

131 is modeled by the SPC/E model. The interaction between oxygen and hydrogen atoms is modeled

132 by the long-range Coulombic potential. The cutoff distance for LJ potential is set as 15 Å. The

133 water molecules are initialized at 1 K in a rectangular box away from the surface and then the

134 temperature is increased to 300 K with an increment of 50 K. Each temperature increment phase

135 is 50 ps. The temperature is maintained at 300 K for another 250 ps to reach equilibrium. The

136 droplet is then brought to the substrate within 3 Angstrom. The spreading and equilibration of the

137 droplet on the surface are for 3 ns. The entire simulation is carried out in the canonical (NVT)

138 ensembles at 300 K using a Nosé-Hoover thermostat. To obtain the statistical droplet profile, we

139 record the positions of water molecules with 1 ps interval in the final 0.2 ns.

2.2 Liquid-gas interface shape model

141 We employ the augmented Young-Laplace equation to account for the entangled effect of

142 surface molecular forces and gas-liquid interface curvature, given as

143
$$P_g - P_l = P_c + P_d, \tag{2}$$

144 where P_d is the disjoining pressure, originating from the surface molecular forces acting on the

145 liquid phase in the equilibrium state [49]. The augmented Young-Laplace equation coupled with

146 various disjoining pressure has been applied in numerous microscopic liquid droplet/film problems

147 [17,50,51]. However, the entangled effect has never been recognized. The main reason is that

148 liquid with infinite size was considered in most cases. In Eq. 2, we consider the entangled effect

149   as a sum of the capillary pressure and the disjoining pressure to determine the liquid-gas interface

150   shape. According to the extended DLVO theory, the disjoining pressure, P_d, mainly includes four

151   components $P_d = P_{vdW} + P_{st} + P_{ha} + P_{dl}$ [25,52,53], where P_{vdW} is the van der Waals force, P_{st}

152   is steric repulsion, P_{ha} is hydrophobic attraction force, P_{ha} is the electrostatic double-layer force.

153   These four components can cover non-covalent interactions, such as for a silicon-water-vapor

154   system [53].

155   Van der Waals force is expressed as $P_{vdW} = -\frac{A}{\delta^3}$ [25,53]. A is the Hamaker constant, which

156   is related to the solid-liquid van der Waals interaction energy by $A = 12\pi\Delta G^{LW} d_0$. ΔG^{LW} is the

157   solid-liquid Lifshitz–van der Waals interaction free energy, d_0 is the minimum equilibrium

158   distance between two condensed-phase surfaces and is considered a constant of 0.157 nm [53].

159   The steric repulsion arises at very small distances to the adsorbed film on a surface. A commonly-

160   used expression of steric repulsion is given by $P_{st} = -\frac{B}{\delta^9}$. B equals to $6A\delta_0^6$ [25]. δ_0 is the

161   thickness of the adsorbed thin film on a given surface. The hydrophobic attraction force can

162   originate when the water molecules near surfaces are induced to order into layers with orientation

163   structure. There is still no universal law for hydrophobic attraction. Here we adopt the expression

164   as $P_{ha} = \Delta G^{AB} e^{-\delta/\lambda} + \Delta G_d^{AB} e^{-\delta/\lambda_d}$ [52,54]. The first term is the short-range hydrophobic force,

165   ΔG^{AB} is the liquid-solid polar interactive free energy. λ is the water characteristic decay length

166   and has to be obtained from experiments. The second term represents the long-range hydrophobic

167   force, whereby ΔG_d^{AB} is considered 1000 times less than ΔG^{AB} according to the previous force

168   measurements [55]. λ_d is by one order of magnitude larger than λ [54]. Electrostatic double-layer

169   force can play a strong role in long-range interactions between electrolytes and a solid surface

170   [56]. However, it exists only between charged molecules (ions) or surfaces and depend on the

171   electrolyte concentration [57]. We examined the contribution of the electrostatic double-layer

172   force to the overall surface molecular forces and found that the electrostatic double-layer force is

173   much weaker compared to other components for the deionized water (A detailed description can

174   be found in the **Supporting Information**). Therefore, we only consider three types of the surface

175   molecular forces, i.e., $P_d = P_{vdW} + P_{st} + P_{ha}$. Note that the disjoining pressure reduces the liquid

176   pressure when it is repulsive.

177   The considered surface molecular forces are defined in terms of solid-liquid-gas interaction

178   free energy ΔG_{slv}. Based on the Dupré equation $\Delta G_{slv} = \gamma_{sl} - \gamma_{sg} - \gamma_{lg}$, we can express the

179   disjoining pressure P_d by interfacial energy γ_{sl}, γ_{sg}, and γ_{lg}. Then, the interfacial energy γ_{sl} can

180   be further related to the surface energy γ_s and γ_l based on the multi-component approach by Oss

181    $\gamma_{sl} = (\sqrt{\gamma_s^{LW}} - \sqrt{\gamma_l^{LW}})^2 + 2(\sqrt{\gamma_s^+} - \sqrt{\gamma_l^+})(\sqrt{\gamma_s^-} - \sqrt{\gamma_l^-})$ [58], where γ_s^{LW}, γ_s^+ and γ_s^- are the

182   Lifshitz–van der Waals surface energy and the polar Lewis acid-base surface energy. Note γ_g is

183   zero in this work. Therefore, the disjoining pressure for a fixed wetting liquid is determined by the

184   surface energy, which can be obtained by measuring the contact angle of three different liquids on

185   the surface. The expression of the disjoining pressure and the derived relationship between

186   interaction free energy and surface energy are summarized in **Table 1**. For the sake of simplicity,

187   we shall name the above-mentioned augmented Young-Laplace equation coupled with the multi-

188   component approach as the **M model.** The calculation methods for the M model can be found in

189   the **Supporting Materials**.

190   The M model provides us with a general mathematical formula to describe the liquid-gas

191   interface profile on any given surface. To validate the M model, we compare the predicted profile

192   by the M model with the MD simulated profile. As shown in **Fig. 2**, a good agreement indicates

193   the validity of the M model for the considered case. Note that the M model cannot capture the

194   details of the droplet profile on the sub-nanoscale. It is because the actual footprint radii of the

195   nano-droplet in MD simulation are difficult to determine when we consider Diaz's approach,

196   which considers a zero slope of the profile at the contact line [59].

197   **Table 1. Components of the M model: disjoining pressure and its relationship with surface**
198   **energy**

Van der Waals force P_{vdW}	$P_{vdW} = -\frac{A}{\delta^3}$ [25]; A: Hamaker constant, $A = 12\pi\Delta G^{LW} d_0$; ΔG^{LW}: liquid-solid Lifshitz-van der Waals interaction free energy;

|	
	d_0 : minimum equilibrium distance between two condensed phase surfaces $= 0.157$ nm [53]
Steric repulsion P_{st}	$P_{st} = -\frac{B}{\delta^9}$ [25]; $B = 6A\delta_0^6$; δ_0 : thickness of the adsorbed thin film on a given surface
Hydrophobic attraction force P_{ha}	$P_{ha} = \Delta G^{AB} e^{-\delta/\lambda} + \Delta G_d^{AB} e^{-\delta/\lambda_d}$ [52,54] ΔG^{AB} : liquid-solid polar interaction free energy; λ: water characteristic decay length; $\Delta G_d^{AB} = \Delta G^{AB}/1000$ [55], $\lambda_d > 10 \lambda$[54] $\Delta G^{AB} e^{-\delta/\lambda}$: short-range hydrophobic force $\Delta G_d^{AB} e^{-\delta/\lambda_d}$: long-range hydrophobic force
Lifshitz-van der Waals interaction free energy ΔG^{LW}	$\Delta G^{LW} = 2[\sqrt{\gamma_s^{LW}\gamma_l^{LW}} + \sqrt{\gamma_g^{LW}\gamma_l^{LW}} - \sqrt{\gamma_s^{LW}\gamma_g^{LW}} - \gamma_l^{LW}]$ [58], γ^{LW}: Lifshitz–van der Waals surface energy
Polar interaction free energy ΔG^{AB}	$\Delta G^{AB} = 2[\sqrt{\gamma_l^+}\left(\sqrt{\gamma_s^-} + \sqrt{\gamma_g^+} - \sqrt{\gamma_l^-}\right) - \sqrt{\gamma_l^-}\left(\sqrt{\gamma_s^+} + \sqrt{\gamma_g^+} - \sqrt{\gamma_v^+}\right) - \sqrt{\gamma_s^+\gamma_g^-} - \sqrt{\gamma_s^-\gamma_g^+}]$ [58], γ^+ and γ^- : the polar Lewis acid-base surface energy

199

200

201
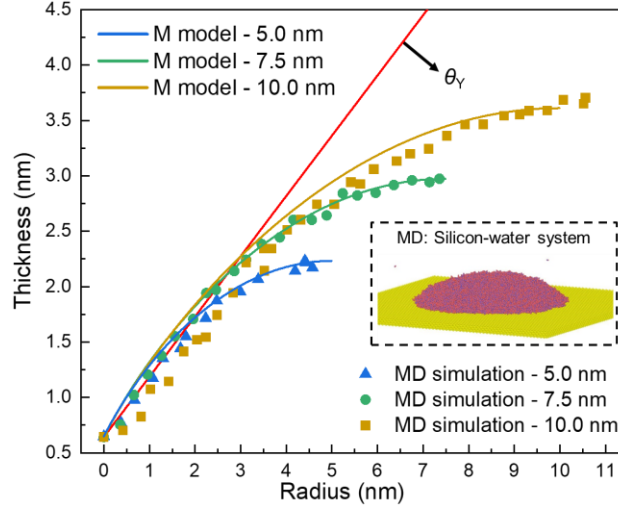
Fig. 2. Comparison of the droplet profiles on the nano-scale obtained from the M model and MD simulation simulations. θ_Y is the Young contact angle of a droplet on a silicon surface [60].

3. Results and discussions

3.1. Deviation of a 3D nano-droplet profile and interface nano-bending

We first start with the deviation of the nano-droplet profile. **Fig. 3a** shows the comparison between the microscopic droplet profile measured on hydroxylated glass in a recent experiment and a spherical shape profile [17]. The spherical shape profile is obtained by fitting the upper part of the droplet profile from the experiment. The microscopic droplet profile shows a deviation from the spherical shape near the contact line within the distance of several nanometers from the surface. This deviation was attributed only to the surface molecular forces [17,20]. **Fig. 3b** gives the sub-nano scale droplet profiles with different footprint radii by using MD simulation. The simulated droplet profiles also exhibit deviation from the spherical shape profile. In this case, the deviation is caused by the entangled effect of surface molecular forces and interface curvature. An interface nano-bending, which shows a concaving pattern on the sub-nanoscale (**Fig. 3b**) and a convex pattern on the nano-scale (**Fig. 2**), is formed near the contact line. This is similar to the experimental measurement as shown in **Fig. 3a**.

To investigate the relationship between the effect of surface molecular forces and the effect of the interface curvature, we compare the droplet profiles obtained by MD simulations and predictions by using Eq. 1 with the boundary condition of the Young contact angle on a silicon surface. From a mechanical perspective, the Young contact angle is defined at an inflection point

222   on the interface of a droplet with infinite size (2D) where the droplet profile transits from concave

223   to convex in the transition region [59]. In the region with a concave profile, surface molecular

224   forces dominate the droplet profile, while in the region with a convex profile, the hydrodynamic

225   effect dominates. Therefore, the Young contact angle can be understood as a manifestation of

226   surface molecular forces near the contact line. The prediction by Eq. 1 for the finite-size droplet

227   (3D) can be interpreted as a linear superposition of the effect of the surface molecular forces and

228   the effect of the local interface curvature on the interface. This method is pure hydrodynamics and

229   has been widely adopted to calculate the droplet or liquid film profile [61,62]. In **Fig. 3b,** the red

230   line represents the profile with infinite droplet size, and dashed lines give the predictions by Eq. 1

231   with the corresponding footprint radii of MD simulations. With the decrease of the footprint radii,

232   the profiles deviate more from the red line because the capillary pressure induced by the larger

233   curvature distorts the interface.

234   However, the droplet profiles by MD simulations deviate more from the red line with the

235   increased footprint radii, which is in contrast to the calculated profiles by Eq. 1. This unexpected

236   result implies the effect of surface molecular forces and the effect of the interface curvature on a

237   3D nano-droplet profile are nonlinearly coupled. In other words, any distortion of the droplet

238   profile caused by one effect simultaneously influences the other one. Thus the interface nano-

239   bending can be understood as a manifestation of the nonlinear-coupled effect near the contact line.

240   The nonlinear-coupled effect may also be influenced by surface heterogeneities and external force

241   fields that can further deform the interface. Therefore, the nonlinear-coupled effect is universal

242   and demands consideration when modeling wetting phenomena.

243   *3.2. Nonlinear-coupled effect*

244   To understand the nonlinear-coupled effect, one must go through the manifestation of surface

245   molecular forces in the interface nano-bending. For example, the 12-6 L-J intermolecular pair

246   potential used in the MD simulation gives rise to surface molecular forces between the liquid-gas

247   interface and the solid-liquid interface [52]. The gas-liquid interface experiences first repulsive

248   force near the surface, and then attractive force when the interface is away from the surface. This

249   qualitative description of the surface molecular forces explains the 3D droplet profile (**Fig. 3b**)

250   obtained by MD simulation very well. However, to answer why the droplet profile deviates more

251   from the red line with the increase of the footprint radii, we need to analyze the role of the interface

252   curvature. Considering an equilibrium droplet, the liquid pressure inside the droplet is uniform.

253   According to Eq. 1, the droplet profile dominated by capillary pressure is convex and with smaller

254   curvature when the footprint radii are larger. Therefore, the role of surface molecular forces and

255   the interface curvature act in opposite ways within the range of repulsive surface molecular forces,

256   while they both act to formulate a convex interface within the range of attractive surface molecular

257   forces. As a result, the droplet profile on the sub-nanoscale deviates more with the increase of the

258   footprint radii. A quantitative description of the nonlinear-coupled effect will rely on the analysis

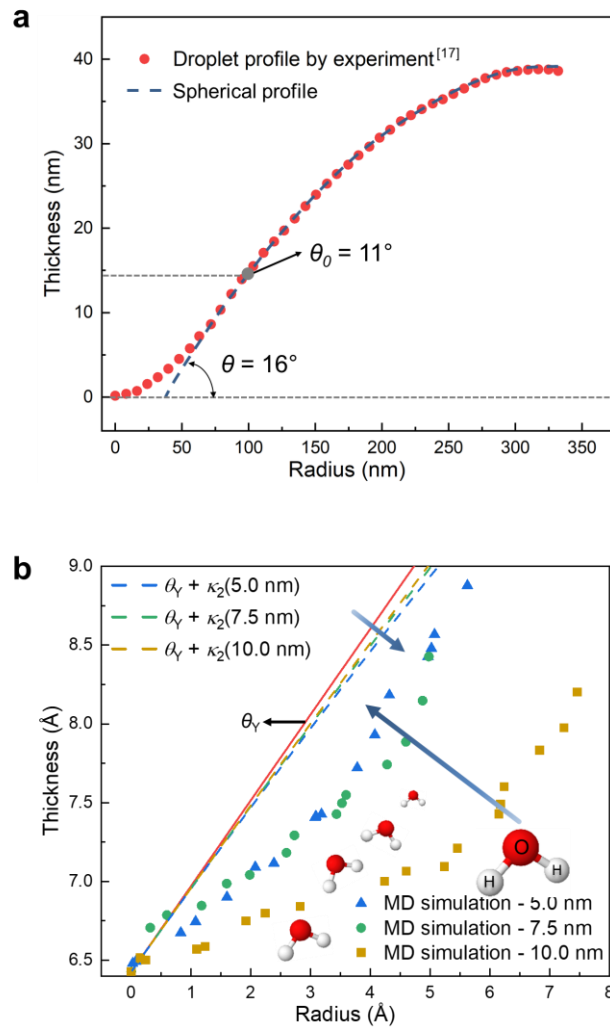259   of the microlayer model in the next sections.

260

261

262   **Fig. 3. Deviation of the 3D nano-droplet profile.** (**a**) Comparison of the nano-droplet profile

263   obtained from the experiment and a spherical shape. θ_0 is the contact angle at the inflection point

264   obtained from the experiment [17]. θ is the contact angle obtained from the spherical shape profile.

265   (**b**) Comparison of the droplet profiles on the sub-nanoscale obtained from the MD simulations

266   and Eq. 1. θ_Y is the Young contact angle of a droplet on a silicon surface, κ_2 is the principal

267   curvature of the interface that is related to the droplet foorprint radii.

268   *3.3. Profile of the microlayer in the inertia-controlled bubble growth stage*

269   We model the microlayer profile in the inertia-controlled stage in nucleate boiling, also

270   referred to as the initial stage [33]. The concept of the inertia-controlled stage was first proposed

271   in a seminal paper by Mikic *et al.* [46]. In this stage, the bubble expands at a constant speed fueled

272   by the overpressure of the vapor because its high internal pressure prevents the evaporation from

273   the surrounding liquid under low superheat. In the last decade, the snapshots of the microlayer

274   profile from several experiments using the laser interferometry method show that the formed

275   microlayer profile remains almost stationary within a very short time (~0.6 ms) after the bubble

276   nucleation [36,44]. This confirms ignorable evaporation from the microlayer at the beginning of

277   the microlayer formation, namely, the inertia-controlled stage. Besides, the extrapolation of the

278   microlayer profile indicates that there is no contact line movement, thus we can assume a no-slip

279   boundary condition. The stationary microlayer allows us to avoid a transient microlayer in the

280   inertia-controlled stage. As also shown in the literature [31], the interface of the microlayer evolves

281   along with a fixed profile. In this work, we focus on the inertia-controlled stage, thus only the

282   nonlinear-coupled effect and the hydrodynamic effect are considered in modeling the microlayer.

283   The nonlinear-coupled effect and the hydrodynamic effect are considered separately. We

284   divide the microlayer into three regions (**Fig. 1b**): a molecular region, a transition region, and a

285   hydrodynamic region. The nonlinear-coupled effect is accounted for in the molecular and

286   transition region. The interface shape in these two regions can be described by Eq. 2. When a

287   hemispherical bubble nucleus is trapped in a cavity with the radius r_c, the required superheat to

288   activate the nucleate boiling is related to r_c [46]. In this work, we use r_c = 2.8 μm, for which the

289   corresponding activation superheat is 12 K. In the transition region, surface molecular forces

290   become less significant compared to the capillary pressure, thus we assume that the transition

291   region ends when the capillary pressure is much larger (*e.g.,* 10 times) than surface molecular

292   forces. The required two initial conditions at the contact line are given as $\delta_0 = 0.157 \; nm$ [53] and

293 $\delta_0' = 0$, representing the adsorbed film thickness and the initial slope of the film profile.
294 Parameters regarding the surface energy used in the M model are listed in **Table 2**.

295 **Table 2. Surface energy components of studied surfaces.**

Surface	γ^{LW} (mJ/m^2)	γ^+ (mJ/m^2)	γ^- (mJ/m^2)	Young CA (degree)	λ[54] (mm)
Glass[63]	38.2	1.2	49	23.80	0.4459
Silicon[60]	38.6	4	33.98	28.14	0.4613
ITO[64]	45.8	0	63.8	12.60	0.3434
Silica[65]	39.0	0.6	56	18.90	0.3871
Weakly hydrophilic	38.6	4	1.9	75.08	1.1256

296 **Fig. 4a** shows the microlayer profiles in the molecular and transition region on glass, silica,
297 ITO, and silicon surfaces, all of which are calculated by the M model. These profiles vary in
298 thickness due to the different surface energy. Nevertheless, we observe a fixed pattern of the
299 profiles on each surface. The profile first exhibits a concaving pattern and then transits to convex
300 with the slope starting to decrease continuously. This is because, within the nano-scale thickness
301 of the microlayer, the repulsive and attractive molecular forces are dominant in turn. Together with
302 the capillary pressure, a strong interface nano-bending presents within several nanometers of
303 thickness, leading to a significant reduction of both profile thickness and slope in the molecular
304 region. Such a nano-bending, analogy to that in the nano-droplet case, is a manifestation of the
305 nonlinear-coupled effect between surface molecular forces and interface curvature. With the
306 increase of the microlayer thickness, surface molecular forces decay rapidly and the capillary
307 pressure becomes dominant, whereas the bending of the profiles becomes less significant,
308 indicating the start of the hydrodynamic region.

309 For the hydrodynamic region of the microlayer, the hydrodynamic effect is dominant. Since
310 the microlayer is very thin, we apply a lubrication approximation in cylindrical coordinates to
311 describe the liquid flow in the microlayer. Here we derive an **H model** based on Nikolayev's
312 approach [66], given as

14

313 $\quad \frac{\partial}{\partial r}[\delta\left(\frac{\delta}{2} + l_s\right)\frac{\partial\sigma}{\partial r} + \delta^2\left(\frac{\delta}{3} + l_s\right)\frac{\partial P_c}{\partial r}] = \mu(u^i - \frac{J}{\rho_L}).$ (3)

314 $\quad l_s$ is the slip length of the liquid-solid interface, which is not considered in the microlayer in the

315 $\quad$ inertia-controlled stage. u^i is the normal interface velocity and is considered to be positive if

316 $\quad$ directed inside the liquid, $\frac{\partial\sigma}{\partial r}$ represents the Marangoni effect, and J is the mass evaporation flux

317 $\quad$ at the interface. Considering the stationary microlayer profile [36] and nearly homogenous

318 $\quad$ distributed temperature along the microlayer interface, $u^i, \frac{\partial\sigma}{\partial r}$, and J can be eliminated. Substitute

319 $\quad$ the expression of the capillary pressure P_c into Eq. 3, the governing equation becomes

320 $\quad \frac{\partial}{\partial r}[\frac{\delta^3}{3}\frac{\partial}{\partial r}(\frac{\delta''}{(1+\delta'^2)^{\frac{3}{2}}} + \frac{\delta'}{r(1+\delta'^2)^{\frac{1}{2}}})\sigma] = 0.$ (4)

321 $\quad$ **Fig. 4a** shows that the slope variation in the transition region is much weaker compared to that

322 $\quad$ in the molecular region. Further, the experimental microlayer profiles [36,44,67] are

323 $\quad$ approximately linear over the micron scale. This indicates the slope variation of the microlayer

324 $\quad$ profile in the hydrodynamic region is very limited. Thus, we integrate Eq. 4 with respect to r and

325 $\quad$ neglect the terms with second and third-order derivatives of δ. Then an analytical solution of Eq.

326 $\quad$ 4 can be easily derived as

327 $\quad \delta = \sqrt[4]{C_1 r^3 + C_2},$ (5)

328 $\quad$ with $C_1 = -\frac{4C}{\sigma}, C_2 = \delta_a^4 + \frac{4C}{\sigma}r_a^3$, and $C = -\frac{\delta_a'\delta_a^3\sigma}{3r_a^2}$. C, C_1, and C_2 are the constants of integration.

329 $\quad$ The subscript a represents an arbitrary position along the microlayer in the hydrodynamic region.

330 $\quad$ Eq. 5 gives the microlayer profile in the hydrodynamic region. The derivation of the analytical

331 $\quad$ solution Eq. 5 is included in the **Supporting Materials**.

332 $\quad$ According to Eq. 5, the microlayer thickness δ and the interface slope δ' at an arbitrary position

333 $\quad$ along the microlayer are required to determine the constants C, C_1, and C_2. Here we develop a

334 $\quad$ **hybrid model** that covers both the M model and H model by approximately matching the transition

335 $\quad$ region and the hydrodynamic region. In other words, the molecular region and the transition region

15

336 are considered the inner boundary for the entire microlayer. We use the calculated results at the

337 out end of the transition region by the M model to determine the constants of integration (see **Table**

338 **S1** in the **Supporting Materials**). For surfaces of glass, silica, ITO, and silicon, C_1 has very close

339 value, this indicates that the slopes of the microlayer profiles are similar on these surfaces.

340 Furthermore, the calculated C_2 is much smaller than C_1, thus C_2 can be ignored given the

341 millimeter-length microlayer. Now Eq. 5 reduces to $\delta = \sqrt[4]{C_1} r^{0.75}$. It has a similar form to

342 Yabuki's expression $\delta = 5.10 \times 10^{-4} r^{0.69}$, which was obtained by fitting their experimental data

343 [38]. **Fig. 4b** displays the microlayer profiles predicted by our hybrid model and the comparison

344 with previous models and experiments [36–38]. The well-known models derived by Cooper and

345 Smirnov follow from different hydrodynamic descriptions yet both relate the microlayer thickness

346 to the bubble growth time [34,35], expressed as $\delta = C \sqrt{\nu t_g}$. The bubble growth time t_g can be

347 related to the bubble growth speed. The constant C is obtained from an experimental fit and is

348 proportional to the bubble growth speed. As shown in **Fig. 4b,** the results largely overestimate the

349 microlayer thickness, that is, the hydrodynamic effect cannot "bend down" the microlayer

350 effectively. The hybrid model successfully predicts the microlayer profile by considering a new

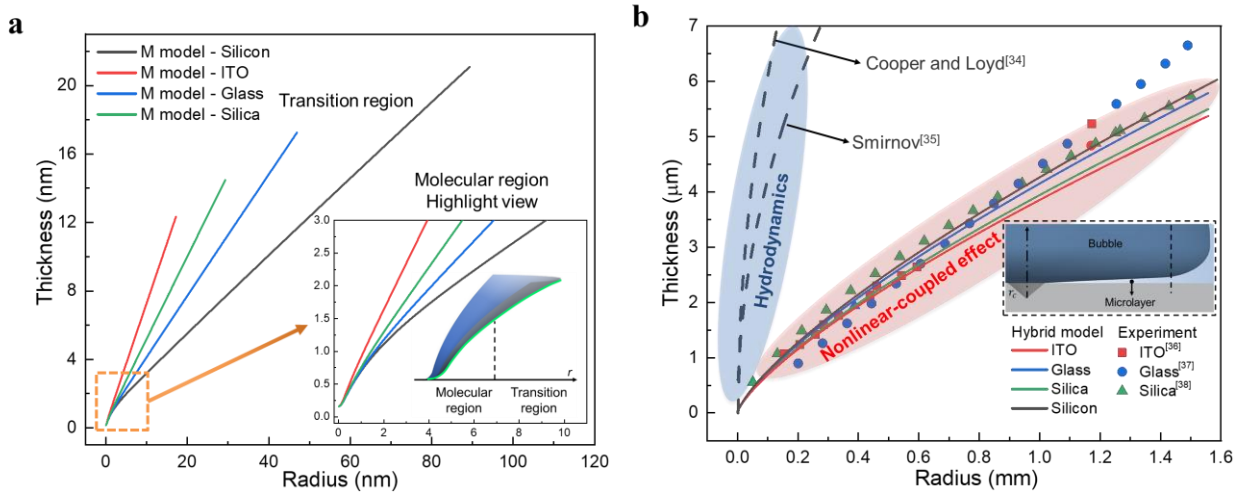351 inner boundary condition, which is derived based on the nonlinear-coupled effect.

352

353 **Fig. 4. Multiscale microlayer profile on various surfaces.** (**a**) Microlayer profiles from the

354 molecular region to the transition region on various surfaces predicted by the M model. (**b**) Full

355 picture of the predicted microlayer profiles by the hybrid model and the comparison with previous

356 models and experiment data. Microlayer profile predictions in the blue region and red region are
357 based on the hydrodynamics and non-linear coupled effect, respectively.

3.4. Deviation of the microlayer profile

359   To understand how the nonlinear-coupled effect formulates the inner boundary condition for
360 the microlayer, we revisit the interface nano-bending in the molecular region (see **Fig. 4a** highlight
361 view). The repulsive surface molecular forces first raise the interface, and consequently, the effect
362 of the second principal curvature κ_2 is enhanced within the thickness of several angstroms. Note
363 that the capillary pressure induced by the second principal curvature increases the liquid pressure,
364 thus preventing the rise of the profile. With the increase in thickness, surface molecular forces turn
365 attractive. Together with the second principal curvature, both act to bend the profile downward.
366 The second principal curvature retards the decay of surface molecular forces and therefore
367 contributes to a further bending of the microlayer profile. The role of the nonlinear-coupled effect
368 differs from that in the nano-droplet. In the case of the microlayer, the coupling effectively
369 strengthens the role of both surface molecular forces and the interface curvature and becomes more
370 powerful in bending the profile.

371   We further consider a linear superposition of the impacts between surface molecular forces
372 and the interface curvature on the profile by bringing each into effect within two consecutive
373 regions starting from the contact line. In the first region, we only consider surface molecular forces
374 and the first principal curvature. We rewrite Eq. 2 as $P_v - P_l = \kappa_1 + P_d$ to describe the microlayer
375 profile. Similar to the interpretation of the Young contact angle of a 2D droplet [59], the Young
376 contact angle is formed in the first region. In the second region, the second principal curvature
377 takes effect and surface molecular forces vanish, the microlayer profile can be described as $P_v -$
378 $P_l = (\kappa_1 + \kappa_2)\sigma$. The boundary between these two regions is where the Young contact angle starts
379 to form in the first region, and the outer end of these two regions is considered to reach the same
380 slope as that at the outer end of the transition region in **Fig. 4a**. In this case, effects of the surface
381 molecular forces and the second principal curvature are linearly superposed, as we discussed in
382 the interpretation of Eq. 1. The calculated results are used to determine C_1 and C_2 in Eq. 5. We
383 show the microlayer profile with and without considering the nonlinear-coupled effect in **Fig. 5a**.
384 The microlayer thickness without the nonlinear-coupled effect reaches around 4.5 µm at 0.5 mm
385 microlayer length, almost 2 times higher than that with the nonlinear-coupled effect.

386   Next, we compare the predicted microlayer profiles with DNS simulations to elucidate the

387   critical role of the inner boundary condition. As shown in **Fig. 5a**, the microlayer profile obtained

388   by Guion *et al.* has a larger thickness [33]. On the other hand, the thickness of the microlayer

389   profile in Ding's work is smaller [31] as there a smaller bubble nucleus size of 2 μm has been

390   assumed compared to the 3 μm in Guion's work. It directly shows the significance of the bubble

391   nucleus size. As indicated by the curvature expression $K = \dfrac{\delta''}{(1+\delta'^2)^{\frac{3}{2}}} + \dfrac{\delta'}{r(1+\delta'^2)^{\frac{1}{2}}}$, the capillary

392   pressure induced by the second principal curvature would be extremely large with the smaller

393   bubble nucleus. Such large capillary pressure can effectively "bend down" the microlayer. In the

394   DNS simulation, the Young contact angle is imposed as the boundary condition, while in our

395   hybrid model, δ'' is also included in the boundary condition and determines the entire microlayer

396   profile implicitly through Eq. 4. The new boundary condition derived based on the nonlinear-

397   coupled effect can be considered as a local pressure boundary condition, which is formulated by

398   the sum of the interface curvature induced capillary pressure and the disjoining pressure in the

399   molecular and transition region. From a perspective of the molecular force, the role of the

400   nonlinear-coupled effect on the macroscale microlayer can be understood as that molecular forces

401   by both water and surface are superimposed on the water-vapor interface in the molecular region

402   and transmitted to the macroscale. In other words, the microlayer profile is a macroscale

403   manifestation of the interaction between the solid surface and water molecules. Nevertheless,

404   numerous previous works have also attempted to incorporate the augmented Young-Laplace

405   equation in the DNS simulation of the microlayer.[41,68–71] Though as we discussed, the

406   augmented Young-Laplace can account for the nonlinear-coupled effect, to the best of our

407   knowledge, there is still no related report of the successful prediction of the microlayer profile.

408   The most important reason is that a rather larger bubble nucleus was employed in these

409   simulations, which overlooked the effect of the interface curvature.

410   Finally, we discuss the microlayer profile on a weakly hydrophilic surface. As shown in **Fig.**

411   **5b**, on a surface with the Young contact angle of 75.08° the microlayer thickness predicted by the

412   hybrid model increases to ~10 μm at 0.5 mm length. Nevertheless, the required cavity radius (*i.e.,*

413   nucleus size) to activate the nucleation is influenced by surface wettability. Previous studies based

414   on thermodynamic analyses suggested a negative correlation between the critical cavity radius and

415   surface wettability [72,73]. Thus, we assume a reduction of the cavity radius r_c on a weakly

416   hydrophilic surface. The results for r_c = 2.8, 1.0, 0.5 μm are plotted in **Fig. 5b**. When r_c decreases

417   the thickness of the microlayer profile decreases too and the actual microlayer profile is met for

418     $r_c = 0.5\ \mu m$. In addition, we can see a stronger impact of the nonlinear-coupled effect on weakly

419   hydrophilic surfaces, because the radii of the second principal curvature are much smaller when
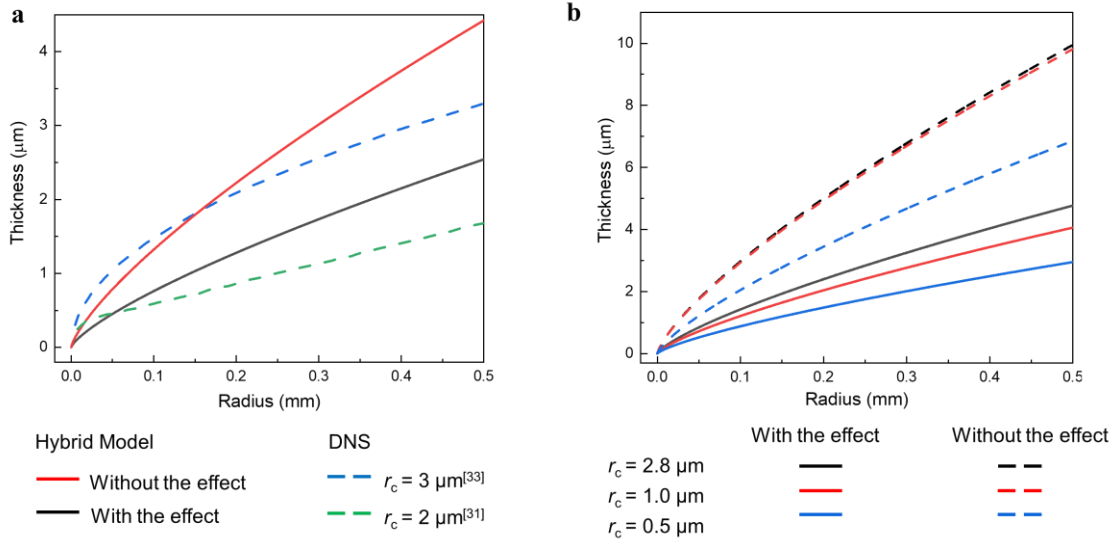
420   the slope of the profile is larger.

421

422   **Fig. 5. Deviation of the microlayer profile.** (**a**) Impact of the nonlinear-coupled effect on

423   microlayer profile and comparison with DNS simulations. The green dashed line is from the

424   simulation of Guion *et al.*; the blue dashed line is from the simulation of Ding *et al.* (**b**) Microlayer

425   profile on the weakly hydrophilic surface with and without the nonlinear-coupled effect (Young

426   contact angle = 75.08°).

427   **4. Conclusions**

428   In this work, we revealed a nonlinear-coupled effect between the liquid-gas interface geometry

429   and the solid-liquid interactions in the microscopic liquid-wetting phenomenon. We performed

430   MD simulations for nano-droplets to examine the nonlinear-coupled effect. Then we applied it in

431   the multiscale modeling (M-Model, H-Model, and hybrid model) of a microlayer in the inertia-

432   controlled bubble growth stage in nucleate boiling. The hybrid model successfully predicted the

433   microlayer profile captured by different experiments [36–38] for the first time. We found that the

434   nonlinear-coupled effect is responsible for the deviation of a nano-droplet profile from the

435   prediction based on the conventional Young contact angle. Furthermore, the very thin microlayer

436 thickness in the inertia-controlled bubble growth stage is determined by the nonlinear-coupled

437 effect, instead of the hydrodynamic effects considered in recent DNS simulation works [33,42,43].

438   The nonlinear-coupled effect explains the mechanism of the microscopic liquid-gas interface

439 deviation from the prediction based on the conventional Young contact angle. We may therefore

440 resolve the long-standing disputes over the validity of the Young contact angle at the nano-scale

441 [28,74,75]. However, the detailed manifestations of the nonlinear-coupled effect depend on the

442 liquid-gas geometries. In the context of the nano-droplet with the principal curvatures of the same

443 signs (spherical shape), the impacts of the interface curvature and the solid-liquid interactions act

444 in the opposite way within the repulsive range of surface molecular forces. In the context of the

445 microlayer with the principal curvatures of the different signs (saddle shape), the nonlinear-

446 coupled effect enhances the impacts of the interface curvature and solid-liquid interactions in

447 bending the microlayer. It indicates that the nonlinear-coupled effect could play a more important

448 role in bubble-related wetting phenomena, such as the long lifetime surface nano-bubble [76].

449 Moreover, the nonlinear-coupled effect structures an interface nano-bending near the surface that

450 can be considered as a new pressure boundary condition for the liquid wetting system. The new

451 pressure boundary condition enables us to unveil mechanisms behind recent intriguing

452 microscopic wetting experiments. For example, the microscopic liquid film evaporation [8], and

453 the surface curvature-driven microscopic droplet motion [6].

454   In future, it would be interesting to reinterpret the line tension based on the nonlinear-coupled

455 effect so that the nonlinear dependency between the cosine of the contact angle of nano-droplets

456 or surface nano-bubbles and the contact line curvature reported in many previous experimental

457 studies [16,77] may be explained.

461 **CRediT authorship contribution statement**

462 **Jinming Zhang:** Conceptualization, Methodology, Validation, Writing - original draft. **Wei Ding:**
463 Conceptualization, Methodology, Writing - review & editing, Supervision. **Zuankai Wang:**

20

Writing – review & editing. **Hao Wang:** Methodology. **Uwe Hampel:** Conceptualization, Methodology, Writing - review & editing, Supervision. All authors have read and agreed to the published version of the manuscript.

Declaration of Competing Interest

The authors declare that they have no known competing financial interests or personal relationships that could have appeared to influence the work reported in this paper.

REFERENCES

[1] J. Hartmann, M.T. Schür, S. Hardt, Manipulation and control of droplets on surfaces in a homogeneous electric field, Nat. Commun. 13 (2022). https://doi.org/10.1038/s41467-021-27879-0.

[2] D. Soltman, B. Smith, S.J.S. Morris, V. Subramanian, Inkjet printing of precisely defined features using contact-angle hysteresis, J. Colloid Interface Sci. 400 (2013) 135–139. https://doi.org/10.1016/j.jcis.2013.03.006.

[3] H. Cha, H. Vahabi, A. Wu, S. Chavan, M.K. Kim, S. Sett, S.A. Bosch, W. Wang, A.K. Kota, N. Miljkovic, Dropwise condensation on solid hydrophilic surfaces, Sci. Adv. 6 (2020). https://doi.org/10.1126/sciadv.aax0746.

[4] X. Dai, N. Sun, S.O. Nielsen, B.B. Stogin, J. Wang, S. Yang, T.S. Wong, Hydrophilic directional slippery rough surfaces for water harvesting, Sci. Adv. 4 (2018) 1–11. https://doi.org/10.1126/sciadv.aaq0919.

[5] S. Feng, P. Zhu, H. Zheng, H. Zhan, C. Chen, J. Li, L. Wang, X. Yao, Y. Liu, Z. Wang, Three-dimensional capillary ratchet-induced liquid directional steering, Science. 373 (2021) 1344–1348. https://doi.org/10.1126/science.abg7552.

486 [6] C. Lv, C. Chen, Y.C. Chuang, F.G. Tseng, Y. Yin, F. Grey, Q. Zheng, Substrate curvature
487   gradient drives rapid droplet motion, Phys. Rev. Lett. 113 (2014) 1–5.
488   https://doi.org/10.1103/PhysRevLett.113.026101.

489 [7] B. Radha, A. Esfandiar, F.C. Wang, A.P. Rooney, K. Gopinadhan, A. Keerthi, A.
490   Mishchenko, A. Janardanan, P. Blake, L. Fumagalli, M. Lozada-Hidalgo, S. Garaj, S.J.
491   Haigh, I. V. Grigorieva, H.A. Wu, A.K. Geim, Molecular transport through capillaries made
492   with   atomic-scale   precision,   Nature.   538   (2016)   222–225.
493   https://doi.org/10.1038/nature19363.

494 [8] Y. Li, M.A. Alibakhshi, Y. Zhao, C. Duan, Exploring Ultimate Water Capillary Evaporation
495   in   Nanoscale   Conduits,   Nano   Lett.   17   (2017)   4813–4819.
496   https://doi.org/10.1021/acs.nanolett.7b01620.

497 [9] D. Jiang, Z. Fan, H. Wang, M. Xu, G. Chen, Y. Song, Z.L. Wang, Triboelectric
498   nanogenerator powered electrowetting-on-dielectric actuator for concealed aquatic
499   microbots, ACS Nano. 14 (2020) 15394–15402. https://doi.org/10.1021/acsnano.0c05901.

500 [10] Y. Wang, S. Gao, W. Xu, Z. Wang, Nanogenerators with Superwetting Surfaces for
501   Harvesting   Water/Liquid   Energy,   Adv.   Funct.   Mater.   30   (2020).
502   https://doi.org/10.1002/adfm.201908252.

503 [11] D. Bonn, J. Eggers, J. Indekeu, J. Meunier, Wetting and spreading, Rev. Mod. Phys. 81
504   (2009) 739–805. https://doi.org/10.1103/RevModPhys.81.739.

505 [12] A. Marmur, Solid-surface characterization by wetting, Annu. Rev. Mater. Res. 39 (2009)
506   473–489. https://doi.org/10.1146/annurev.matsci.38.060407.132425.

507 [13] H. Wang, From Contact Line Structures to Wetting Dynamics, Langmuir. 35 (2019) 10233–

508   10245. https://doi.org/10.1021/acs.langmuir.9b00294.

509 [14] A. Moldovan, P.M. Bota, T. Dan Poteca, I. Boerasu, D. Bojin, D. Buzatu, M. Enachescu,

510   Scanning polarization force microscopy investigation of contact angle and disjoining

511   pressure of glycerol and sulfuric acid on highly oriented pyrolytic graphite and aluminum,

512   EPJ Appl. Phys. 64 (2013) 1–7. https://doi.org/10.1051/epjap/2013130235.

513 [15] T. Pompe, S. Herminghaus, Three-phase contact line energetics from nanoscale liquid

514   surface   topographies,   Phys.   Rev.   Lett.   85   (2000)   1930–1933.

515   https://doi.org/10.1103/PhysRevLett.85.1930.

516 [16] A. Checco, P. Guenoun, J. Daillant, Nonlinear dependence of the contact angle of

517   nanodroplets   on   contact   line   curvature,   Phys.   Rev.   Lett.   91   (2003)   1–4.

518   https://doi.org/10.1103/PhysRevLett.91.186101.

519 [17] F. Samoila, L. Sirghi, Disjoining Pressure in Partial Wetting on the Nanoscale, Langmuir.

520   33 (2017) 5188–5196. https://doi.org/10.1021/acs.langmuir.7b01156.

521 [18] P.C. Wayner Jr, The effect of interfacial mass transport on flow in thin liquid films, Colloids

522   and Surfaces. 52 (1991) 71–84. http://www.scopus.com/inward/record.url?eid=2-s2.0-

523   0026060309&partnerID=40&md5=050cabcb8304a02f45dc463caca00df7.

524 [19] S. Narayanan, A.G. Fedorov, Y.K. Joshi, Interfacial transport of evaporating water confined

525   in nanopores, Langmuir. 27 (2011) 10666–10676. https://doi.org/10.1021/la201807a.

526 [20] P.G.D. Gennes, X. Hua, P. Levinson, Dynamics of wetting: Local contact angles, J. Fluid

527   Mech. 212 (1990) 55–63. https://doi.org/10.1017/S0022112090001859.

528   [21]   H. Wang, L. Chen, A general model for dynamic contact angle over full speed regime,

529   ArXiv. (2019) 4–6.

530   [22]   Z. Lu, S. Narayanan, E.N. Wang, Modeling of Evaporation from Nanopores with

531   Nonequilibrium and Nonlocal Effects, Langmuir. 31 (2015) 9817–9824.

532   https://doi.org/10.1021/acs.langmuir.5b01700.

533   [23]   R.J. Good, M.N. Koo, The effect of drop size on contact angle, J. Colloid Interface Sci. 71

534   (1979) 283–292. https://doi.org/10.1016/0021-9797(79)90239-X.

535   [24]   J. Park, H.S. Han, Y.C. Kim, J.P. Ahn, M.R. Ok, K.E. Lee, J.W. Lee, P.R. Cha, H.K. Seok,

536   H. Jeon, Direct and accurate measurement of size dependent wetting behaviors for sessile

537   water droplets, Sci. Rep. 5 (2015) 1–13. https://doi.org/10.1038/srep18150.

538   [25]   A. Setchi, Y. Chen, J. Yu, H. Wang, Structural effects in partially-wetting thin evaporating

539   liquid films near the contact line, Int. J. Heat Mass Transf. 132 (2019) 420–430.

540   https://doi.org/10.1016/j.ijheatmasstransfer.2018.11.151.

541   [26]   L. Schimmele, M. Naplórkowski, S. Dietrich, Conceptual aspects of line tensions, J. Chem.

542   Phys. 127 (2007). https://doi.org/10.1063/1.2799990.

543   [27]   M. Kanduč, L. Eixeres, S. Liese, R.R. Netz, Generalized line tension of water nanodroplets,

544   Phys. Rev. E. 98 (2018) 1–6. https://doi.org/10.1103/PhysRevE.98.032804.

545   [28]   J. Zhang, P. Wang, M.K. Borg, J.M. Reese, D. Wen, A critical assessment of the line tension

546   determined by the modified Young's equation, Phys. Fluids. 30 (2018).

547   https://doi.org/10.1063/1.5040574.

548   [29]   A. Amirfazli, A.W. Neumann, Status of the three-phase line tension: A review, Adv. Colloid
549   Interface Sci. 110 (2004) 121–141. https://doi.org/10.1016/j.cis.2004.05.001.

550   [30]   J. Kim, Review of nucleate pool boiling bubble heat transfer mechanisms, Int. J. Multiph.
551   Flow. 35 (2009) 1067–1076. https://doi.org/10.1016/j.ijmultiphaseflow.2009.07.008.

552   [31]   W. Ding, J. Zhang, D. Sarker, U. Hampel, The role of microlayer for bubble sliding in
553   nucleate boiling: A new viewpoint for heat transfer enhancement via surface engineering,
554   Int. J. Heat Mass Transf. 149 (2020) 119239.
555   https://doi.org/10.1016/j.ijheatmasstransfer.2019.119239.

556   [32]   D.I. Yu, H.J. Kwak, H. Noh, H.S. Park, K. Fezzaa, M.H. Kim, Synchrotron x-ray imaging
557   visualization study of capillary-induced flow and critical heat flux on surfaces with
558   engineered micropillars, Sci. Adv. 4 (2018) 3–6. https://doi.org/10.1126/sciadv.1701571.

559   [33]   A. Guion, S. Afkhami, S. Zaleski, J. Buongiorno, Simulations of microlayer formation in
560   nucleate boiling, Int. J. Heat Mass Transf. 127 (2018) 1271–1284.
561   https://doi.org/10.1016/j.ijheatmasstransfer.2018.06.041.

562   [34]   M.G. Cooper, A.J.P. Lloyd, The microlayer in nucleate pool boiling, Int. J. Heat Mass
563   Transf. 12 (1969) 895–913. https://doi.org/10.1016/0017-9310(69)90154-9.

564   [35]   G.F. Smirnov, Calculation of the "initial" thickness of the "microlayer" during bubble
565   boiling, J. Eng. Phys. 28 (1975) 369–374. https://doi.org/10.1007/BF00862021.

566   [36]   S. Jung, H. Kim, Hydrodynamic formation of a microlayer underneath a boiling bubble, Int.

567   J. Heat Mass Transf. 120 (2018) 1229–1240.

568   https://doi.org/10.1016/j.ijheatmasstransfer.2017.12.098.

569   [37] Y. Utaka, Y. Kashiwabara, M. Ozaki, Microlayer structure in nucleate boiling of water and

570   ethanol at atmospheric pressure, Int. J. Heat Mass Transf. 57 (2013) 222–230.

571   https://doi.org/10.1016/j.ijheatmasstransfer.2012.10.031.

572   [38] T. Yabuki, O. Nakabeppu, Heat transfer mechanisms in isolated bubble boiling of water

573   observed with MEMS sensor, Int. J. Heat Mass Transf. 76 (2014) 286–297.

574   https://doi.org/10.1016/j.ijheatmasstransfer.2014.04.012.

575   [39] S. Hänsch, S. Walker, Microlayer formation and depletion beneath growing steam bubbles,

576   Int. J. Multiph. Flow. 111 (2019) 241–263.

577   https://doi.org/10.1016/j.ijmultiphaseflow.2018.11.004.

578   [40] G. Giustini, S. Jung, H. Kim, K.H. Ardron, S.P. Walker, Microlayer evaporation during

579   steam bubble growth, Int. J. Therm. Sci. 137 (2019) 45–54.

580   https://doi.org/10.1016/j.ijthermalsci.2018.11.012.

581   [41] J. Bhati, S. Paruya, Numerical simulation of bubble dynamics in pool boiling at heated

582   surface, Int. J. Heat Mass Transf. 152 (2020) 119465.

583   https://doi.org/10.1016/j.ijheatmasstransfer.2020.119465.

584   [42] A. Urbano, S. Tanguy, G. Huber, C. Colin, Direct numerical simulation of nucleate boiling

585   in micro-layer regime, Int. J. Heat Mass Transf. 123 (2018) 1128–1137.

586   https://doi.org/10.1016/j.ijheatmasstransfer.2018.02.104.

587   [43]   L. Bureš, Y. Sato, On the modelling of the transition between contact-line and microlayer

588   evaporation regimes in nucleate boiling, J. Fluid Mech. 916 (2021) 1–23.

589   https://doi.org/10.1017/jfm.2021.204.

590   [44]   Z. Chen, A. Haginiwa, Y. Utaka, Detailed structure of microlayer in nucleate pool boiling

591   for water measured by laser interferometric method, Int. J. Heat Mass Transf. 108 (2017)

592   1285–1291. https://doi.org/10.1016/j.ijheatmasstransfer.2017.01.003.

593   [45]   M. Gao, L. Zhang, P. Cheng, X. Quan, An investigation of microlayer beneath nucleation

594   bubble by laser interferometric method, Int. J. Heat Mass Transf. 57 (2013) 183–189.

595   https://doi.org/10.1016/j.ijheatmasstransfer.2012.10.017.

596   [46]   B.B. Mikic, W.M. Rohsenow, P. Griffith, On bubble growth rates, Int. J. Heat Mass Transf.

597   13 (1970) 657–666. https://doi.org/10.1016/0017-9310(70)90040-2.

598   [47]   S. Plimpton, Fast Parallel Algorithms for Short-Range Molecular Dynamics, J. Comput.

599   Phys. 117 (1995) 1–19. https://doi.org/10.1006/jcph.1995.1039.

600   [48]   B. Ramos-Alvarado, S. Kumar, G.P. Peterson, Wettability of graphitic-carbon and silicon

601   surfaces: MD modeling and theoretical analysis, J. Chem. Phys. 143 (2015).

602   https://doi.org/10.1063/1.4927083.

603   [49]   B. V. Derjaguin, N. V. Churaev, On the question of determining the concept of disjoining

604   pressure and its role in the equilibrium and flow of thin films, J. Colloid Interface Sci. 66

605   (1978) 389–398. https://doi.org/10.1016/0021-9797(78)90056-5.

606   [50]   I. V. Kuchin, O.K. Matar, R. V. Craster, V.M. Starov, Influence of the Disjoining Pressure

607   on the Equilibrium Interfacial Profile in Transition Zone Between a Thin Film and a

608   Capillary Meniscus, Colloids Interface Sci. Commun. 1 (2014) 18–22.

609   https://doi.org/10.1016/j.colcom.2014.06.002.

610   [51]   J.A. Schonberg, S. DasGupta, P.C. Wayner, An augmented Young-Laplace model of an

611   evaporating meniscus in a microchannel with high heat flux, Exp. Therm. Fluid Sci. 10

612   (1995) 163–170. https://doi.org/10.1016/0894-1777(94)00085-M.

613   [52]   J.N. Israelachvili, Intermolecular and Surface Forces, 3rd ed., Elsevier, 2011.

614   https://linkinghub.elsevier.com/retrieve/pii/C20090215601.

615   [53]   C.J. van Oss, The Properties of Water and their Role in Colloidal and Biological Systems,

616   1st ed., Academic Press, 2008.

617   [54]   N. V. Churaev, V.D. Sobolev, Wetting of low-energy surfaces, Adv. Colloid Interface Sci.

618   134–135 (2007) 15–23. https://doi.org/10.1016/j.cis.2007.04.012.

619   [55]   M.U. Hammer, T.H. Anderson, A. Chaimovich, M.S. Shell, J. Israelachvili, The search for

620   the hydrophobic force law, Faraday Discuss. 146 (2012) 299–308.

621   https://www.ncbi.nlm.nih.gov/pmc/articles/PMC3624763/pdf/nihms412728.pdf.

622   [56]   O. Arjmandi-Tash, N.M. Kovalchuk, A. Trybala, I. V. Kuchin, V. Starov, Kinetics of

623   Wetting and Spreading of Droplets over Various Substrates, Langmuir. 33 (2017) 4367–

624   4385. https://doi.org/10.1021/acs.langmuir.6b04094.

625   [57]   A. Majumdar, I. Mezic, Instability of ultra-thin water films and the mechanism of droplet

626   formation on hydrophilic surfaces, J. Heat Transfer. 121 (1999) 964–971.

627   https://doi.org/10.1115/1.2826087.

628 [58] C.J. Van Oss, Long-range and short-range mechanisms of hydrophobic attraction and

629   hydrophilic repulsion in specific and aspecific interactions, J. Mol. Recognit. 16 (2003)

630   177–190. https://doi.org/10.1002/jmr.618.

631 [59] M. Elena Diaz, J. Fuentes, R.L. Cerro, M.D. Savage, An analytical solution for a partially

632   wetting puddle and the location of the static contact angle, J. Colloid Interface Sci. 348

633   (2010) 232–239. https://doi.org/10.1016/j.jcis.2010.04.030.

634 [60] D.J. Preston, Y. Song, Z. Lu, D.S. Antao, E.N. Wang, Design of Lubricant Infused Surfaces,

635   ACS   Appl.   Mater.   Interfaces.   9   (2017)   42383–42392.

636   https://doi.org/10.1021/acsami.7b14311.

637 [61] P.D. Ravazzoli, I. Cuellar, A.G. González, J.A. Diez, Contact-angle-hysteresis effects on a

638   drop   sitting   on   an   incline   plane,   Phys.   Rev.   E.   99   (2019)   043105.

639   https://doi.org/10.1103/PhysRevE.99.043105.

640 [62] V. Janeček, V.S. Nikolayev, Contact line singularity at partial wetting during evaporation

641   driven by substrate heating, Epl. 100 (2012). https://doi.org/10.1209/0295-5075/100/14003.

642 [63] A. Kowalski, Z. Czech, Ł. Byczyński, How does the surface free energy influence the tack

643   of acrylic pressure-sensitive adhesives (PSAs)?, J. Coatings Technol. Res. 10 (2013) 879–

644   885. https://doi.org/10.1007/s11998-013-9522-2.

645 [64] E.M. Harnett, J. Alderman, T. Wood, The surface energy of various biomaterials coated

646   with adhesion molecules used in cell culture, Colloids Surfaces B Biointerfaces. 55 (2007)

647   90–97. https://doi.org/10.1016/j.colsurfb.2006.11.021.

648   [65]   D. Aronov, G. Rosenman, Surface energy modification by electron beam, Surf. Sci. 601

649   (2007) 5042–5049. https://doi.org/10.1016/j.susc.2007.09.003.

650   [66]   V.S. Nikolayev, Dynamics of the triple contact line on a nonisothermal heater at partial

651   wetting, Phys. Fluids. 22 (2010). https://doi.org/10.1063/1.3483558.

652   [67]   S. Jung, H. Kim, An experimental method to simultaneously measure the dynamics and heat

653   transfer associated with a single bubble during nucleate boiling on a horizontal surface, Int.

654   J. Heat Mass Transf. 73 (2014) 365–375.

655   https://doi.org/10.1016/j.ijheatmasstransfer.2014.02.014.

656   [68]   G. Son, V.K. Dhir, N. Ramanujapu, Dynamics and heat transfer associated with a single

657   bubble during nucleate boiling on a horizontal surface, J. Heat Transfer. 121 (1999) 623–

658   631. https://doi.org/10.1115/1.2826025.

659   [69]   D.M. Christopher, L. Zhang, Heat transfer in the microlayer under a bubble during nucleate

660   boiling, Tsinghua Sci. Technol. 15 (2010) 404–413. https://doi.org/10.1016/S1007-

661   0214(10)70080-8.

662   [70]   E. Aktinol, V.K. Dhir, T. Jaeger, W. Mirczak, Numerical simulations of nucleate boiling

663   and film condensation heat transfer in a fixed-volume chamber in microgravity, Int. J. Heat

664   Mass Transf. 132 (2019) 886–905.

665   https://doi.org/10.1016/j.ijheatmasstransfer.2018.11.125.

666   [71]   V.K. Dhir, G.R. Warrier, E. Aktinol, Numerical simulation of pool boiling: A review, J.

667   Heat Transfer. 135 (2013). https://doi.org/10.1115/1.4023576.

668 [72] X. Quan, G. Chen, P. Cheng, A thermodynamic analysis for heterogeneous boiling

669   nucleation on a superheated wall, Int. J. Heat Mass Transf. 54 (2011) 4762–4769.

670   https://doi.org/10.1016/j.ijheatmasstransfer.2011.05.026.

671 [73] S.G. Bankoff, Entrapment of gas in the spreading of a liquid over a rough surface, AIChE

672   J. 4 (1958) 24–26. https://doi.org/10.1002/aic.690040105.

673 [74] D. Seveno, T.D. Blake, J. De Coninck, Young's equation at the nanoscale, Phys. Rev. Lett.

674   111 (2013). https://doi.org/10.1103/PhysRevLett.111.096101.

675 [75] T. Ingebrigtsen, S. Toxvaerd, Contact angles of Lennard-Jones liquids and droplets on

676   planar   surfaces,   J.   Phys.   Chem.   C.   111   (2007)   8518–8523.

677   https://doi.org/10.1021/jp0676235.

678 [76] D. Lohse, X. Zhang, Surface nanobubbles and nanodroplets, Rev. Mod. Phys. 87 (2015)

679   981–1035. https://doi.org/10.1103/RevModPhys.87.981.

680 [77] N. Kameda, S. Nakabayashi, Size-induced sign inversion of line tension in nanobubbles at

681   a   solid/liquid   interface,   Chem.   Phys.   Lett.   461   (2008)   122–126.

682   https://doi.org/10.1016/j.cplett.2008.07.012.

683

684